International Journal of Heat and Mass Transfer 147 (2020) 119022

Contents lists available at ScienceDirect

International Journal of Heat and Mass Transfer

journal homepage: www.elsevier.com/locate/hmt

Numerical simulations of the liquid-vapor phase change dynamic processes in a flat micro heat pipe

Wen-Zhen Fang[a,b,*], Yu-Qing Tang[a], Chun Yang[b], Wen-Quan Tao[a]

[a] Key Laboratory of Thermo-Fluid Science and Engineering, MOE, Xi'an Jiaotong University, Xi'an, China
[b] School of Mechanical and Aerospace Engineering, Nanyang Technological University, Singapore

ARTICLE INFO

Article history:
Received 23 June 2019
Revised 19 October 2019
Accepted 8 November 2019
Available online 15 November 2019

Keywords:
Phase change
Lattice Boltzmann method
Capillary force
Flat micro heat pipe
Pore scale

ABSTRACT

The performance of a flat micro heat pipe (FMHP) is highly dependent on the wick geometry. Understanding the dynamic behaviors of liquid-vapor phase change in the FMHP is of significance for its optimal design, especially the wick geometry. In this work, a pore-scale three-dimensional pseudopotential lattice Boltzmann model coupled with a thermal model is developed to study the transient behaviors of the FMHP without any empirical equations. In the developed model, the curvature of liquid-vapor meniscus can be automatically adjusted according to the external heat source and the receding behavior of liquid films can be captured. Besides, effects of detailed wick microstructures on the performance of the FMHP are systematically studied. The results show that a more hydrophilic grooved wick yields a higher capillary force to improve the working ability. The working temperature and liquid charge amount significantly affect the performance of the FMHP. The grooved-type wick with a trapezoid shape has the best performance, next by the rectangular shape and then inversed trapezoid shape. For the micro-pillar type wick, with a relatively small pillar pitch at the evaporation section and a large pitch at the condensation section can improve the working performance.

1. Introduction

With the downsizing of electronic devices, the efficient heat dissipation in the electronic device plays a significant role in avoiding the overheating which can dramatically reduce the performance and lifespan of the device [1, 2]. The heat pipe has proven to be an efficient passive cooling tool for thermal devices, which behaves as a medium that can transfer heat from local hot spots to the environment. The miniature heat pipes used in the electronic devices are mostly defined as the flat micro heat pipe (FMHP) [3]. Taking advantages of the large amount of latent heat during the phase change, the heat flux of the heat pipe can be several orders of magnitude higher than those of metal conductors, such as aluminum and copper [4].

The heat pipe modellings are still challenging due to the coupled mechanisms, including heat, mass and momentum transports, together with the evaporation and condensation in the wick. The strong coupling between the temperature, pressure and velocity at the liquid-vapor interface imposes a great difficulty in the modelling. Due to the much effort devoted in the past decades, a variety of numerical and analytical models have been developed to model the transport processes inside a heat pipe. Although the analytical models can provide some physical insights, they did have limitations since the partial differential governing equations always do not have analytical results and thus many assumptions are needed [5, 6].

Alternatively, many authors resort to the numerical modellings to directly resolve the coupled heat transfer and fluid flow processes inside the heat pipes. The previous numerical models can be divided into two categories: steady state models [7-9] and transient models [10]. Compared with the steady state, heat pipes operating at the transient state are more complex since the liquid-vapor interface and phase change rate are all dynamic. Dynamic behavior of heat pipes is an important factor to evaluate their performance, especially when they are operating at the start-up period or experiencing a sudden heat load situation. In this work, a transient numerical model is developed to study the coupled fluid flow and heat transfer process of the heat pipe.

In recent decades, many studies have been conducted on the numerical modeling of transient performance of heat pipes. Specifically, the finite volume model [10], the thermal network approach [11] and the lumped vapor model [12,13] were developed to capture the dynamic behaviors of a heat pipe when responses to the sudden increase of the heat input. Moreover, the

* Corresponding author at: Key Laboratory of Thermo-Fluid Science and Engineering, MOE, Xi'an Jiaotong University, Xi'an, China.
E-mail address: fangwenzhen76@gmail.com (W.-Z. Fang).

https://doi.org/10.1016/j.ijheatmasstransfer.2019.119022
0017-9310/

Nomenclature

Variables

c_s	Lattice sound speed
d	Pillar space (mm)
D	Diffusivity (m^2/s)
$\boldsymbol{e}$	Discrete velocity (m/s)
f	Density distribution function
F	Force (N)
h_{lv}	Latent heat (kg/m^3)
H	Wick height (mm)
L	Length (m)
G	Interaction strength
Q	Heat transport rate (K)
P	Pressure (Pa)
r	Radius of the curvature
R	Universal gas constant (J/mol/K)
$\boldsymbol{x}$	Position (m)
T	Temperature (K)
t	Time (s)
u	Fluid velocity (m/s)
W	Wick width (mm)

Greek

$\boldsymbol{\Lambda}$	Collision matrix
θ	Contact angle (°)
ω	weight parameter
ε	Porosity
ρ	fluid density (kg/m^3)
λ	Thermal conductivity (W/(m·K))
ϕ	Source term
δ	Fin thickness (mm)
τ	Relaxation coefficient
μ	Dynamic viscosity (Pa·s)

Subscript

c	Critical
h	High
i	ith direction
l	Low
s	Saturation

three-dimensional finite volume models were developed to analyze the transient performance of heat pipes subjected to multiple discrete heat sources [14], non-uniform heat source [15] and thermal cycle duration [16]. Besides, to determine the evaporation/condensation rate on the liquid-vapor interface, the kinetic theory in conjunction with Clausius–Clapeyron equation is always adopted to simulate the transient performance of the heat pipe [17, 18].

Most of previous models predict the thermal performance of heat pipes at different operating conditions by neglecting the curvature effect of meniscus at the liquid–vapor interface. However, if the size of heat pipe is at the micro scale, the detailed thermal and mass transport will become sensitive to the capillary force which is determined by the curvature of the liquid–vapor interface. In this regard, Rice and Faghri [19], and Ranjan et al. [17, 20] have paid much effort to consider the effects of curvature of menisci to predict the capillary limit of the heat pipe. However, they assumed that the interface was stationary and the interface profile was predetermined according to the pressure difference [17, 19] or surface energy [20], which would result in the loss of important physical insights, such as the receding of the liquid film and adjustment of curvature of liquid meniscus in response to the external heat source. Besides, the value of accommodation coefficients in the kinetic theory to determine phase change rate is reported to vary several orders of magnitude [21], leading to the inaccuracy of the numerical model.

In this work, a three-dimensional (3D) liquid-vapor phase change lattice Boltzmann (LB) model is developed to investigate the transient behaviors of a FMHP. With the developed model, the curvature of liquid-vapor meniscus can be automatically adjusted according to the external heat source and receding behavior of liquid films can be captured, which avoids the assumption that the wicks must be saturated in the previous studies [22, 23]. Besides, due to the kinetic nature of LB model, the phase change rate at the liquid-vapor interface can be determined by the interaction between liquid phase and vapor phase, and thus no more gas kinetic theory is needed to determine the interfacial mass flux. The first liquid-vapor phase change LB model was proposed by Házi and Márkus [24] to investigate the boiling heat transfer, and then further improved by Gong and Cheng [25]. Furthermore, Fang et al. [26] modified the thermal LB model and proposed a suitable treatment for conjugate heat transfer to investigate the pool boiling at a larger liquid-vapor density ratio.

The previous studies always neglect effects of wick microstructures on the dynamic transport behaviors of heat pipes by assuming the porous wick structures as the continuum media [14-16], which need empirical models to obtain effective transport properties of porous wicks to close the model. In contrast, the pore scale modeling can provide the detailed flow dynamic and heat transfer inside the wick, which can help elucidate how the wick structure affects the performance of the FMHP. In this regard, Mottet et al. [27] and Nishikawara et al. [28] developed a 3D pore network model to investigate the fluid flow and heat transfer in a loop heat pipe. Besides, Li et al. [29] adopted the LBM to study effects of heat flux and wick wettability on the patterns and dynamics of liquid-vapor interface of a loop heat pipe.

Since the LBM has a great advantage in dealing with the complex boundaries [30-34], it is adopted in this work to investigate the coupled multiphase flow and heat transfer in the FMHP at the pore scale. The present 3D LB model can take any wick structure as the geometry input, thus making it possible to address the structure-related performance of heat pipe. The microstructure of the wick is highly related to the working performance of the heat pipe. With the development in the advanced manufacturing technology, the grooved-type wicks [35, 36] and micro-pillar type wicks [37, 38] are preferred for the FMHP. In this work, effects of the wick microstructure on the dynamic thermal performance of the FMHP are investigated and the performance of the FMHP is improved by optimizing the wick microstructures.

This rest of this paper is organized as follows. The liquid-vapor phase change LB model and boundary conditions are presented in Section 2. Effects of the wettability, working temperature, working liquid charge amount, geometries of grooved wicks and thermal performance of pillar-type wicks are studied in Section 3. Finally, several conclusions are drawn in Section 4.

2. Numerical method

2.1. MRT LBM for multiphase flow

Multi-relation-time LB model has a better stability and accuracy than the single-relation-time models. In this study, a three-dimensional nineteen-velocity (D3Q19) LB model with the MRT collision operator is employed. The evolution of the LB equation for each distribution function is as follows

$$f_\alpha(\boldsymbol{x}+\boldsymbol{e}_\alpha\delta t, t+\delta t) - f_\alpha(\boldsymbol{x}, t) = -\left(\mathbf{M}^{-1}\Lambda\mathbf{M}\right)_{\alpha\beta}\left[f_\beta - f_\beta^{eq}\right] + \delta t F'_\alpha \quad (1)$$

where $f(\boldsymbol{x}, t)$ is the density distribution function at the lattice site $\boldsymbol{x}$ and time t; δt is the time step; and $f^{eq}$is the corresponding equilibrium distribution function; and $\boldsymbol{e}_\alpha$ is the discrete velocity along the α direction, given by:

$$\boldsymbol{e}_\alpha = \begin{bmatrix} 0,1,-1,0,0,0,0,1,-1,1,-1,1,-1,1,-1,0,0,0,0 \\ 0,0,0,1,-1,0,0,1,1,-1,-1,0,0,0,0,1,-1,1,-1 \\ 0,0,0,0,0,1,-1,0,0,0,0,1,1,-1,-1,1,1,-1,-1 \end{bmatrix} \quad (2)$$

With an orthogonal transformation matrix $\mathbf{M}$, Eq. (1) can be mapped into the moment space and has the expression as:

$$\boldsymbol{m}^* = \boldsymbol{m} - \boldsymbol{\Lambda}(\boldsymbol{m} - \boldsymbol{m}^{eq}) + \delta_t\left(\mathbf{I} - \frac{\boldsymbol{\Lambda}}{2}\right)\boldsymbol{S} \quad (3)$$

where $\boldsymbol{m} = \mathbf{M}\boldsymbol{f}$ and $\boldsymbol{m}^{eq} = \mathbf{M}\boldsymbol{f}^{eq}$, while $\boldsymbol{m}^{eq}$ is defined as

$$\boldsymbol{m}^{eq} = \rho\begin{pmatrix} 1, -11 + 19(u_x^2+u_y^2+u_z^2), 3 - \frac{11}{2}(u_x^2+u_y^2+u_z^2), \\ u_x, -\frac{2}{3}u_x, u_y, -\frac{2}{3}u_y, u_z, -\frac{2}{3}u_z, \frac{1}{2}(2u_x^2 - u_y^2 - u_z^2), \\ u_y^2 - u_z^2, \frac{1}{2}(u_y^2 - u_z^2), u_xu_y, u_xu_z, 0, 0, 0 \end{pmatrix}^T \quad (4)$$

$\boldsymbol{\Lambda}$ is the diagonal collision matrix, given by

$$\Lambda = diag(\tau_0^{-1}, \tau_e^{-1}, \tau_\varepsilon^{-1}, \tau_0^{-1}, \tau_q^{-1}, \tau_0^{-1}, \tau_q^{-1}, \tau_0^{-1}, \tau_q^{-1}, \tau_\nu^{-1}, \tau_\pi^{-1}, \tau_\nu^{-1}, \tau_\pi^{-1}, \tau_\nu^{-1}, \tau_\nu^{-1}, \tau_\nu^{-1}, \tau_t^{-1}, \tau_t^{-1}, \tau_t^{-1}) \quad (5)$$

In Eq. (3), $\boldsymbol{S}$ is the forcing term in the moment space with $(\mathbf{I} - \boldsymbol{\Lambda}/2)\boldsymbol{S} = \mathbf{M}\boldsymbol{F}'$. Following the studies presented in Ref. [39-41], an improved forcing term should be adopted to achieve the thermodynamic consistency:

$$\boldsymbol{S} = \begin{pmatrix} 0, 38(u_xF_x + u_yF_y + u_zF_z) + 114\varepsilon\left(F_x^2 + F_y^2 + F_z^2\right)/(\psi^2(\tau_e - 0.5)), \\ -11(u_xF_x + u_yF_y + u_zF_z), F_x, -2/3F_x, F_y, -2/3F_y, F_z, -2/3F_z, \\ 2(2u_xF_x - u_yF_y - u_zF_z), -2u_xF_x + u_yF_y + u_zF_z, 2(u_yF_y - u_zF_z), \\ -u_yF_y + u_zF_z, u_xF_y + u_yF_x, u_yF_z + u_zF_y, u_xF_z + u_zF_x, 0, 0, 0 \end{pmatrix}^T \quad (6)$$

where ε is a parameter used to improve the thermodynamic consistency and is determined to be 0.093 by a series of preliminary test. In Eq. (6), the total force $\boldsymbol{F}$ includes fluid-fluid cohesion forces $\boldsymbol{F}_f$, fluid-solid adhesion forces $\boldsymbol{F}_s$ and gravitational force $\boldsymbol{F}_g$, of which the fluid-fluid cohesion forces can be obtained as follows

$$\boldsymbol{F}_f = -G_f\psi(\boldsymbol{x})c_s^2\sum_{\alpha=1}^{18}\omega\left(|\boldsymbol{e}_\alpha|^2\right)\psi(\boldsymbol{x} + \boldsymbol{e}_\alpha\delta t)\boldsymbol{e}_\alpha \quad (7)$$

where G_f reflects the interaction strength among fluids; $\omega(|\boldsymbol{e}_\alpha|^2)$ is the weight parameter, and ψ is the effective mass or the pseudopotential, which is defined as

$$\psi(\boldsymbol{x}) = \sqrt{\frac{2\left(P - \rho c_s^2\right)}{G_f c_s^2}} \quad (8)$$

In the present paper, the P-R equation of state is adopted to describe thermodynamic state of the fluids

$$P = \frac{\rho RT}{1 - b\rho} - \frac{a\beta(T)\rho^2}{1 + 2b\rho - b^2\rho^2} \quad (9)$$

with

$$\beta(T) = \left[1 + \left(0.37464 + 1.54226\omega - 0.2699\omega^2\right) \times \left(1 - \sqrt{T/T_c}\right)\right]^2 \quad (10.a)$$

$$a = 0.45724(RT_c)^2/P_c,\ b = 0.1873RT_c/P_c \quad (10.b)$$

where T_c and P_c are the critical temperature and critical pressure, respectively. In this study, we choose $a = 2/49$, $b = 2/21$, $\omega = 0.344$.

The fluid-solid adhesion forces can be calculated by

$$\boldsymbol{F}_s = -G_s\psi(\boldsymbol{x})c_s^2\sum_{\alpha=1}^{18}\omega\left(|\boldsymbol{e}_\alpha|^2\right)\psi(\rho_w)s(\boldsymbol{x} + \boldsymbol{e}_\alpha\delta t)\boldsymbol{e}_\alpha \quad (11)$$

where $s(\boldsymbol{x} + \boldsymbol{e}_\alpha\delta t)$is an indicator function which is 1 for solid and 0 for fluid phase; ρ_w is the virtual wall density, which is a free parameter used to tune the wettability of the wall.

The gravitational force is:

$$\boldsymbol{F}_g = (\rho - \rho_{ave})\boldsymbol{g} \quad (12)$$

where ρ_{ave} is the average fluid density of the entire computational domain, and $\boldsymbol{g}$ is the gravitational acceleration.

2.2. LBM for heat transfer

The energy transport equation can be expressed as follows [25,26]

$$\rho c_v\frac{dT}{dt} = \nabla\cdot(\lambda\nabla T) - T\left(\frac{\partial P_{EOS}}{\partial T}\right)\nabla\cdot\mathbf{u} \quad (13)$$

For convenience, a single-relaxation-time LB model is adopted in this study to solve the energy equation

$$h_i(\boldsymbol{x} + \boldsymbol{e}_i\delta_t, t + \delta_t) - h_i(\boldsymbol{x}, t) = -\frac{1}{\tau_T}\left[h_i(\boldsymbol{x}, t) - h_i^{eq}(\boldsymbol{x}, t)\right] + \delta_t\omega_i\phi \quad (14)$$

where the equilibrium temperature distribution function has an expression as:

$$h_i^{eq} = \omega_i T\left[1 + \frac{\boldsymbol{e}_i\cdot\mathbf{u}}{c_s^2} + \frac{(\boldsymbol{e}_i\cdot\mathbf{u})^2}{2c_s^4} - \frac{\mathbf{u}^2}{2c_s^2}\right] \quad (15)$$

By Chapman-Enskog expansion, this LB model retrieves the following advection-diffusion energy equation

$$\frac{\partial T}{\partial t} + \nabla\cdot(\mathbf{u}T) = \nabla\cdot(D\nabla T) + \phi \quad (16)$$

where ϕ is the source term. Compared with the form of Eq. (16), Eq. (13) can be rewritten as [26]

$$\frac{\partial T}{\partial t} + \nabla\cdot(\mathbf{u}T) = \nabla\cdot(D\nabla T) - \nabla\left(\frac{1}{\rho c_v}\right)\cdot(\lambda\nabla T) + T\left[1 - \frac{1}{\rho c_v}\left(\frac{\partial P_{EOS}}{\partial T}\right)\right]\nabla\cdot\mathbf{u} \quad (17)$$

where the second term on the right side of Eq. (17) is the additional source term due to the variable ρc_v in the computational domain while the third term is the source term due to the phase change.

2.3. Boundary condition and computational domain

The working efficiency of the FMHP is highly related to the microstructure of the hydrophilic wick. One representative unit cell of the FMHP with a rectangular-grooved wick is shown in Fig. 1. The size of the computational domain is $300(L_x) \times 100(L_y) \times 150(L_z)$, with each grid denoting 6 μm. The thickness of the solid substrate is set to be 10 lattice grids. The depth, width and fin thickness of the rectangular grooved wick are denoted as H, W and δ, respectively, as shown in Fig. 1. Along the x direction, the FMHP is evenly divided into three subregions as the evaporation section, condensation section and adiabatic section. Initially, the charge amount of the working liquid is just equal to the height of the wick. For

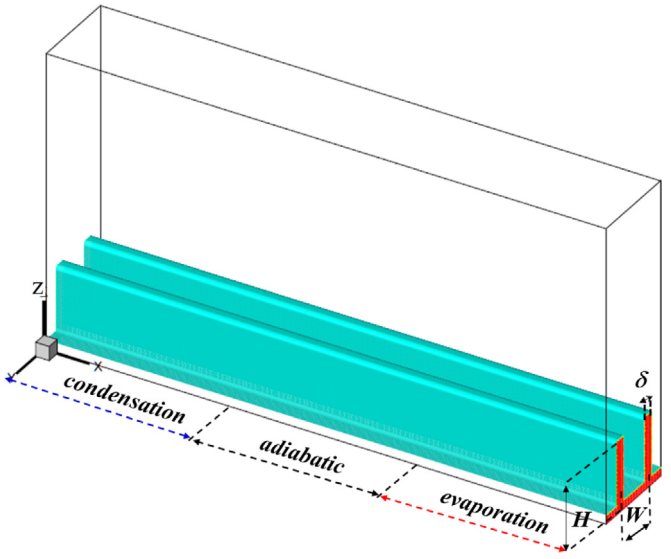

Fig. 1. Microstructures and computational domain of a flat micro heat pipe with the rectangular grooved wick.

boundary conditions in simulations, the periodic conditions are assigned in y direction, while other boundaries are set to be wall (no slip for fluid flow and adiabatic condition for heat transfer).

In this model, an equation of state (EOS) of the real fluid, is needed to simulate dynamic evaporation and condensation at the liquid-vapor interfaces and potential receding of working liquids into the wick when subjected to the external heat source. In this work, a widely used P-R EOS is adopted to capture the phase change of the water. Due to the limitation of the Shan-Chen pseudopotential LB model, the density ratio of liquid and vapor cannot be very large, especially when it is coupled with the thermal LB model. Although several studies have been conducted to increase the liquid-vapor density ratio, it remains a challenge when fluids work in porous media. In this work, the saturation temperature of working fluid is set to be $T_s = 0.86\ T_c$, where T_c is the critical temperature, and thus the liquid-vapor density ratio of the working fluid is about 17. Note that a modest liquid-vapor density ratio would lead to a relatively small latent heat, which can further affect the working performance of the heat pipe, such as the heat transport limitation and calculated heat flux. However, the modest density ratio does not affect the current model to capture the phenomena where dynamic liquid-vapor interfaces are receded into wicks and even dried out when subjected to the external heat source. Thus, the underlying physics and optimization of the wick geometry obtained in this work are not affected by such modest liquid-vapor density ratio.

3. Results and discussion

To compare the LB results with experimental data or the analytical models, the lattice unit should be converted into the physical unit. Thus, one should ensure the following dimensionless number calculated by the lattice unit and physical unit is identical:

$$Ca = \frac{\mu Q}{\sigma \rho A h_{lv}} \tag{18}$$

where μ is the dynamic viscosity of liquid; Q is the heat transport rate; σ is the surface tension; A is the area of the cross section; h_{lv} is the latent heat related to the liquid-vapor phase change.

The effectiveness and accuracy of the present liquid-vapor phase change LB model have been properly validated in our previous studies [26,42]. For brevity, we did not again present the code validation in this work. The maximum heat transfer rate with the rectangular groove can be predicted using the following equation [43]:

$$Q_m = \frac{2\sigma/W}{\mu_l/(KA\rho h_{fg})(L_e/2 + L_c/2 + L_a)} \tag{19}$$

where W is the width of groove; K is the permeability of the wick; L_e, L_c and L_a are the length of evaporation section, condensation section and adiabatic section, respectively. Due to the relatively short length of heat pipe studied in this work (1.8 mm) compared to its typical length in the order of 10^{-1} m, the calculated heat flux limitations (see Figs. 5, 6, 9, 11) are approximately two orders larger than the typical values.

3.1. Effects of wettability

The wick in the FMHP is designed to be hydrophilic to absorb the working liquid from the condensation section into evaporation section to avoid the dry out of the working fluid in evaporation section. The wettability of the wick is highly related to its working efficiency. Fig. 2 shows the effects of the wettability of the wick on the working process of a FMHP with the rectangular grooved wick. Here, the evaporation section is subjected to a high temperature environment $T_h = 0.89\ T_c$ while the condensation section is subjected to a low temperature environment $T_l = 0.83\ T_c$. The working liquid in the evaporation section is transformed into vapor by absorbing heat from the high temperature environment, while the vapor in the condensation section condenses into liquid by releasing heat into the low temperature environment. Due to the capillary effect, the working liquid in the condensation section can be sucked into the evaporation section to feed the working liquid for continuous evaporation. Thus, the working fluid in the evaporation section with $\theta = 85°$ is easily drying out due to its smallest capillary driven force, while the amount of working fluid in the evaporation section with $\theta = 60°$ can maintain unchanged when subjected to such environmental condition.

The pressure profiles of liquid and vapor along the x direction (flow direction of working fluid) at different wettability of wicks are shown in Fig. 3. It can be seen that the pressure difference between the liquid and vapor in the evaporation section is larger than that in the condensation section, and such difference increases with the wettability of the hydrophilic wick. According to Laplace's law:

$$\Delta P_{lv} = \frac{\sigma}{r} = \frac{\sigma \cos\theta}{2W} \tag{20}$$

where r is the radius of the curvature. As shown in Fig. 2, a higher wettability of wick causes a larger curvature of the liquid-vapor interface at the evaporation section. Besides, the curvature of the liquid-vapor interface at the condensation section is reduced and can even be flat since the vapor is condensed at the liquid-vapor interface. Thus, the capillary pressure difference between the evaporation section and condensation section drives the working liquid flow back into the evaporation section to avoid the liquid at the evaporation section drying out. The difference of ΔP_{lv} increases with the wettability of wicks. This is the reason why the case of $\theta = 60°$ has a better ability to avoid the drying out of working fluid at the evaporation section.

3.2. Effects of working temperatures

The performance of the heat pipe is highly dependent on the working temperature. The working fluid at the evaporation section can be receded into wick and even drying out when subjected to the external heat source. Fig. 4 shows the effects of the working temperature on the performance of the FMHP. At a relatively

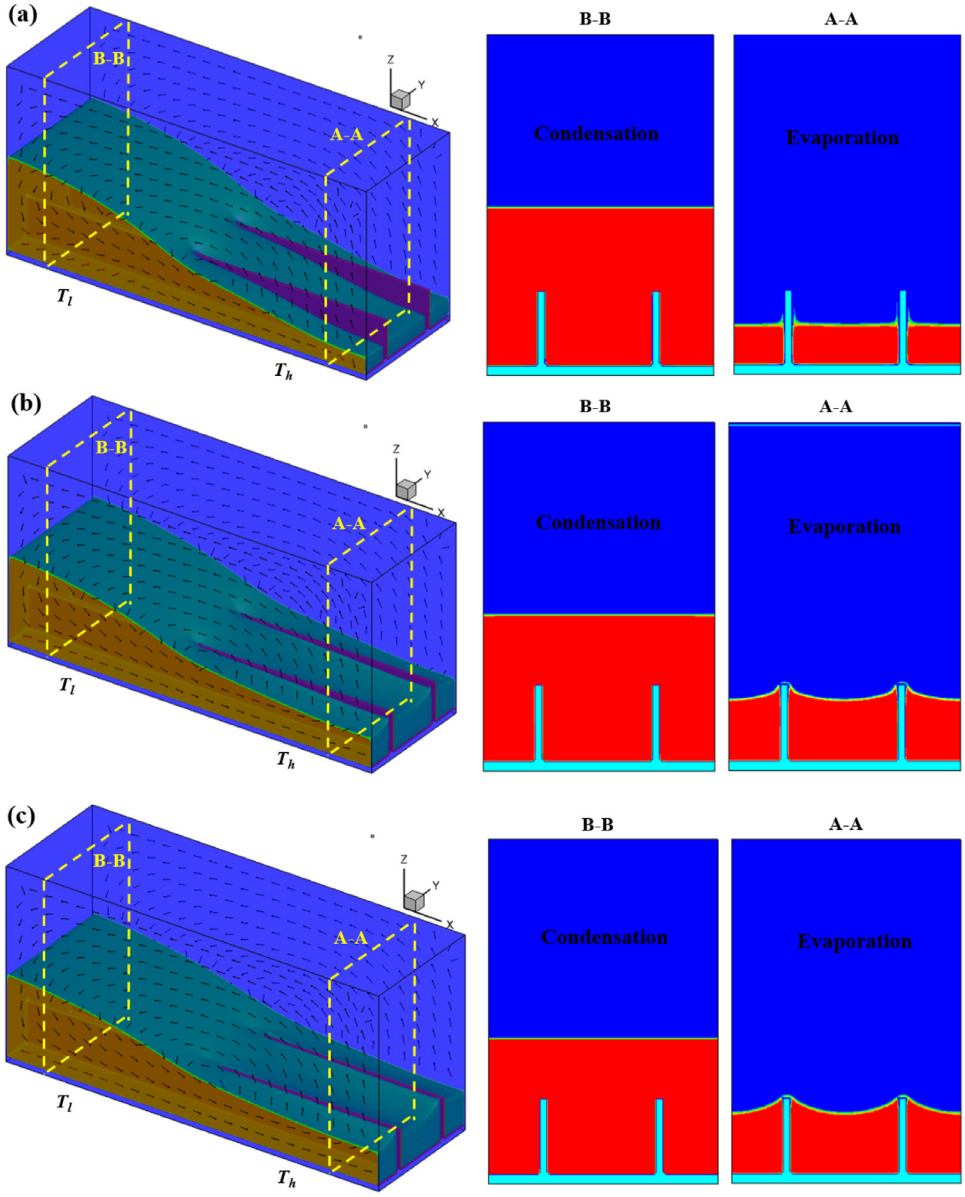

Fig. 2. Fluid flow (arrow direction) and fluid distributions in the FMHP with the rectangular grooved wick at different wettability (a) contact angle $\theta = 85°$ (b) $\theta = 70°$ (c) $\theta = 60°$ (time instant $t = 1.8\,s$; blue: vapor, red: liquid; color images can be seen in the online version).

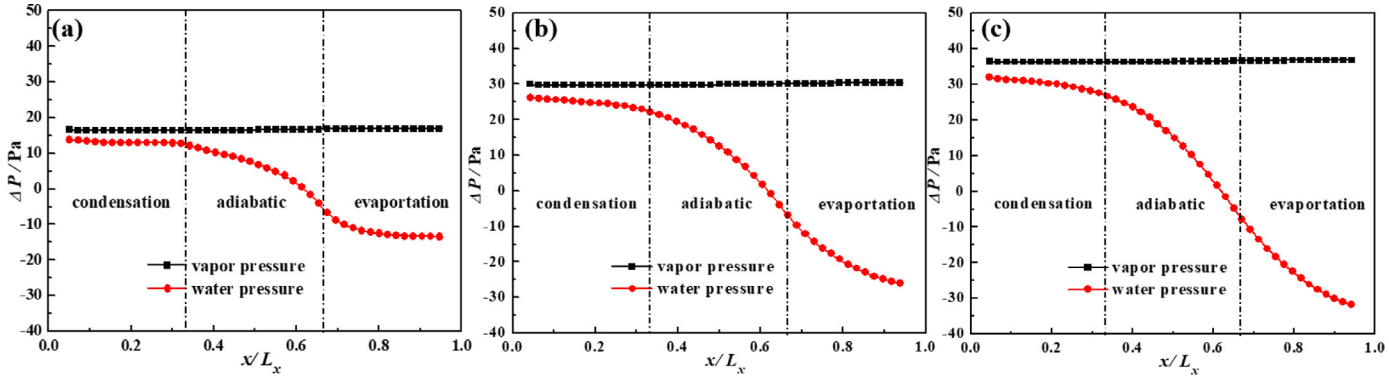

Fig. 3. Pressure profiles of liquid and vapor along the flow direction (x-direction) in a FMHP at different wettability of rectangular grooved wicks (a) $\theta = 85°$ (b) $\theta = 70°$ (c) $\theta = 60°$ ($\Delta P = P\text{-}P_{ref}$, P_{ref} is the reference pressure; time instant $t = 1.8\,s$).

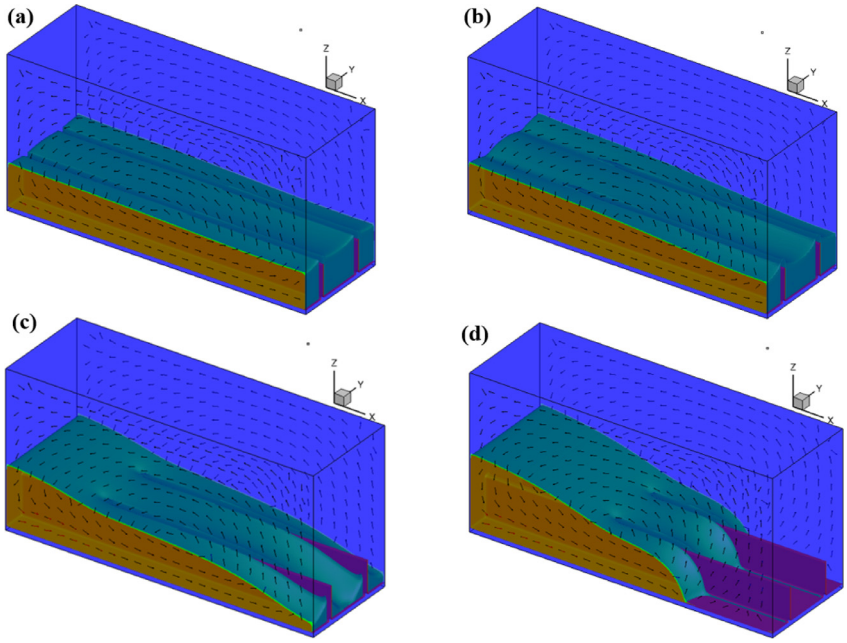

Fig. 4. Effects of working temperatures on the performances of the heat pipe (a) $T_h = 0.88\ T_c$, $T_l = 0.84\ T_c$, $t = 3.1$ s; (b) $T_h = 0.90\ T_c$, $T_l = 0.82\ T_c$, $t = 3.1$ s; (c) $T_h = 0.92\ T_c$, $T_l = 0.80\ T_c$, $t = 1.1$ s; (d) $T_h = 0.92\ T_c$, $T_l = 0.80\ T_c$, $t = 3.1$ s (Saturation temperature $T_s = 0.86\ T_c$).

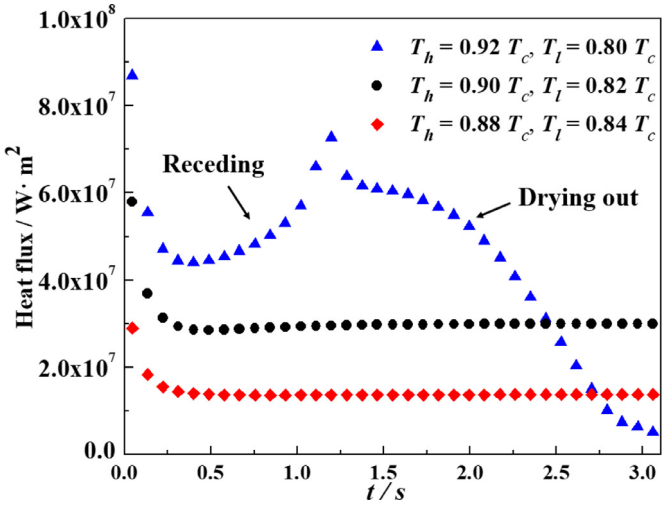

Fig. 5. Variations of the averaged heat flux versus time at different working temperature.

low working temperature ($T_h = 0.88\ T_c$, $T_l = 0.84\ T_c$), the evaporation and condensation rate of working fluid are rather low, resulting in an almost unchanged profile of the working fluid compared with the initial state. On the contrary, the evaporation rate and condensation rate are intensified at the higher working temperature ($T_h = 0.92\ T_c$, $T_l = 0.80\ T_c$). The dynamic liquid-vapor interface is receded into the groove wick to provide the necessary capillary force to drive back the working fluid at the condensation section. When the heat flux exceeds the capillary limit, the drying out the working fluid at the evaporation section will happen, as shown in Fig. 4(d).

Fig. 5 shows the variation of the averaged heat flux versus time at different working temperature. The calculated heat flux is averaged on the entire evaporation section. In can be seen that the heat pipe can reach a quasi-static state when works on the relatively low temperature ($T_h = 0.90\ T_c$ and $T_h = 0.88\ T_c$). However, when it works at the high temperature ($T_h = 0.92\ T_c$), the working liquid at the evaporation section rapidly recedes into the grooved wick due to the evaporation, resulting in the reduction of liquid film at the evaporation section. The reduction in the liquid film reduces the heat transfer resistance, which leads to the increase of the heat flux. However, since the working fluid cannot meet the evaporation rate, the drying out of the working fluid at the evaporation section will occur. When a portion of evaporation section starts to dry out, the averaged heat flux will decrease due to the amount reduction of liquid-vapor phase change which can absorb large amount of heat. From the curve shown in Fig. 5, we can tell that the drying out of working fluid starts to appear around $t = 1.25$ s.

3.3. Effects of liquid charge amount

In this section, the effect of the liquid charge amount on the thermal performance of the heat pipe are investigated, and its influences on the thermal performance of the heat pipe with the rectangular grooved wick are shown in Fig. 6. The heights of the rectangular grooved wick are $h = 0.18$ mm and $h = 0.24$ mm for Fig. 6(a) and (b), respectively. Initially, the rectangular grooved wick is saturated with the working fluid. In these cases, the working temperature are $T_h = 0.88\ T_c$, $T_l = 0.84\ T_c$ for the evaporation and condensation sections. Fig. 6(c) shows the variation of calculated heat fluxes versus time. It can be seen that the heat flux of the wick height $h = 0.18$ mm is larger than that of $h = 0.24$ mm at the steady state. Because the evaporation is occurred at the liquid-vapor interfaces, the main thermal resistance is the conduction of liquid film on the surface, thus resulting in the decrease of the heat flux of $h = 0.24$ mm. On the other hand, if the liquid charge amount is too low, the working fluid at the evaporation section is easily to be dried out. Therefore, the liquid charge amount at the heat pipe should be carefully designed according to the environment requirement.

3.4. Effects of geometries of the grooved wick

The performance of the heat pipe is highly related to the wick geometry. In this section, the effects of microstructures of the

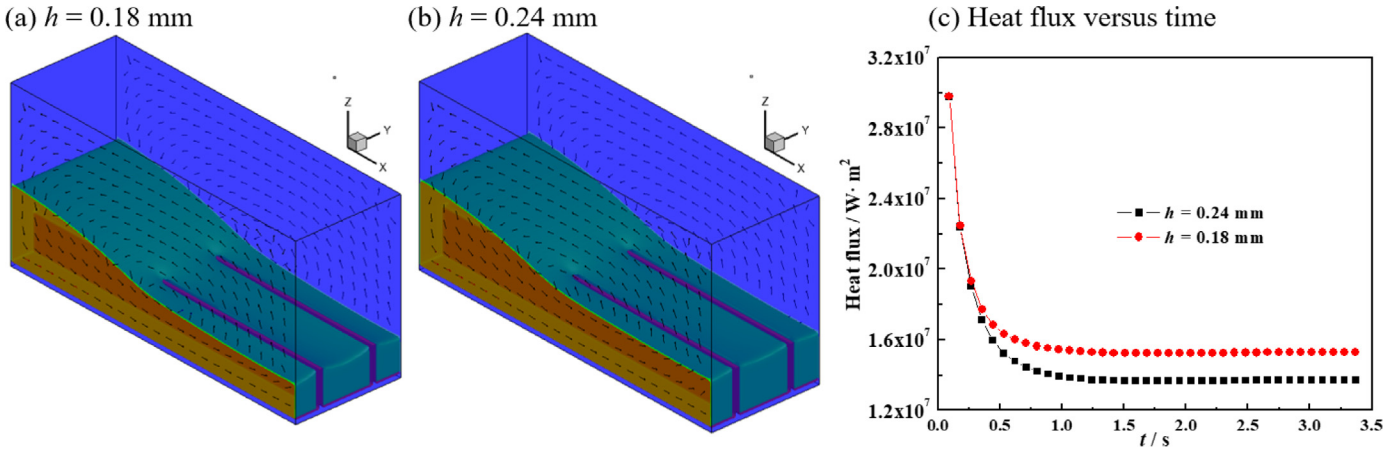

Fig. 6. Thermal performances of the heat pipe at different liquid charge amounts (a) wick height $h = 0.18$ mm (b) wick height $h = 0.24$ mm (c) heat flux versus time (time instant $t = 3.1$ s; working temperature $T_h = 0.88\ T_c$, $T_l = 0.84\ T_c$).

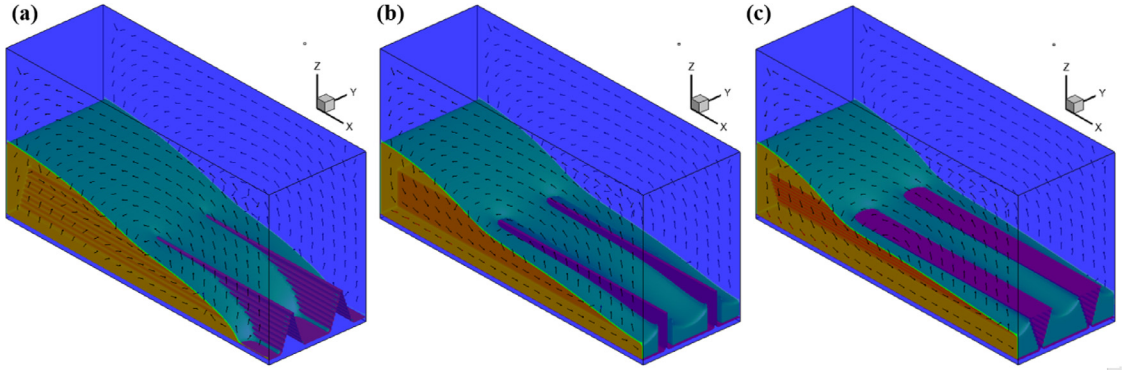

Fig. 7. Effects of the geometries of grooved wicks on the performance of the heat pipe (a) inversed trapezoidal groove (b) rectangular groove (c) trapezoidal groove ($t = 3.25$ s).

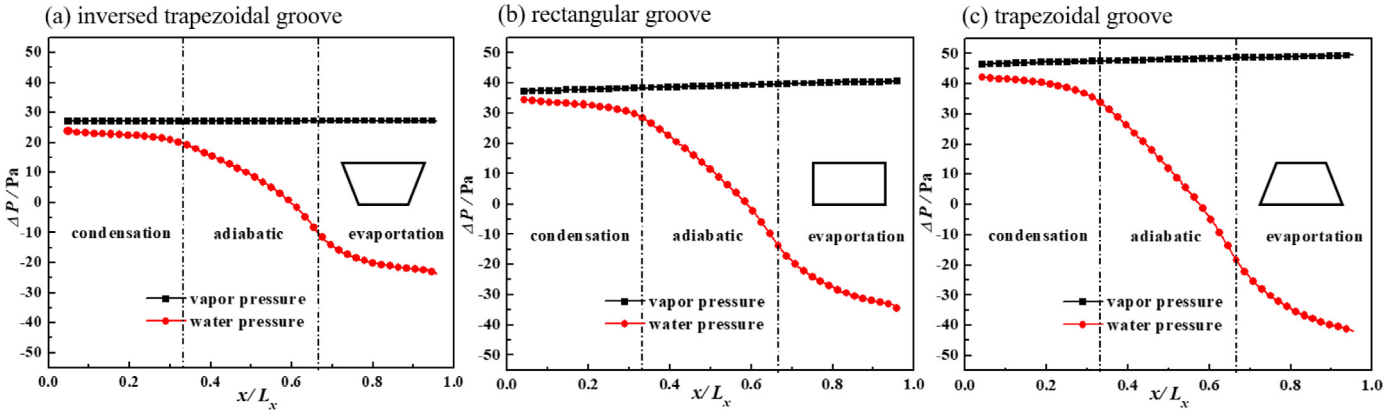

Fig. 8. Liquid and vapor pressures along the flow direction of working fluids in a heat pipe with different geometries of the grooved wicks (a) inversed trapezoidal groove (b) rectangular groove (c) trapezoidal groove ($\Delta P = P\text{-}P_{ref}$, P_{ref} is the reference pressure; time instant $t = 2.2$ s).

grooved wick on the thermal performance of the heat pipe are studied. The studied microstructures of the grooved wick include: inversed trapezoidal groove, rectangular groove and trapezoidal groove. Here, the working temperature are set to be $T_h = 0.90\ T_c$, $T_l = 0.82\ T_c$, and the contact angle of wicks is 60°. The areas of the cross section and heights of grooved wicks are set to be identical in this work. At the time instant $t = 3.25$ s, working fluids distributions for different geometries of the grooved wicks are illustrated in Fig. 7. It can be seen that the trapezoidal groove can maintain the working fluid in the evaporation section, while the working fluid is receded into the wick for the rectangular groove and even dries out for the inversed trapezoidal groove. The pressure profiles of liquid and vapor along the flow direction at different geometries of the grooved wicks are shown in Fig. 8. It can be seen that the pressure difference between the liquid and vapor at the evaporation section is the largest for the trapezoidal groove geometry, while the lowest for the inversed trapezoidal groove geometry. Due to the geometry effect, the trapezoidal groove has a smallest gap at the top among three geometries, thus resulting in the largest pressure difference between the liquid and vapor. Thus, the wick with the trapezoidal groove type has the largest capillary force to suck the working fluid from the condensation section to avoid the

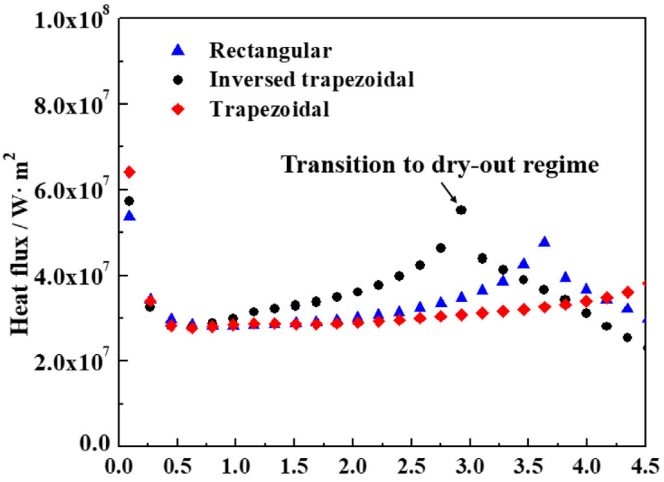

Fig. 9. Variations of the averaged heat flux versus time at different wick geometries (heat flux is averaged on the entire evaporation section).

drying out of the working fluid at the evaporation section. Such observations are in consistence with the previous analytical results [43,44].

Fig. 9 shows the comparisons of averaged heat flux among different wick geometries. We can see that the wick with inversed trapezoidal groove has the superior heat flux at the early time due to the relatively thinner liquid film but decreases rapidly due to the easily drying out of the working fluid. The peak heat flux denotes the transition point from the receding regime to the dry-out regime of the working fluid. The moments of drying out of working fluids happens at $t \approx 2.8$ s for the inversed trapezoidal grooved wick, while $t \approx 3.6$ s for the rectangular groove. On the contrary, the dry-out regime is not occurred for the trapezoidal grooved wick.

3.5. Thermal performance of pillar-type wicks

Apart from the grooved-type wicks, the pillar-type hydrophilic wicks are also widely used. In this section, two kinds of the pillar-type wicks are investigated: evenly-spaced pillar-type wick and unevenly-spaced pillar-type wick, as shown in Fig. 10. For the evenly-spaced pillar-type wicks, the studied pillar pitches (d) are set to be 0.06 mm, 0.12 mm and 0.18 mm, respectively; while for the unevenly-spaced wick, the pillar is dense at the evaporation section and sparse at the condensation section, with pillar pitch of 0.06 mm and 0.18 mm, respectively. Initially, the wicks are saturated with working fluids.

Effects of the pillar configuration on the performance of the heat pipe are shown in Fig. 11. Here, the working temperature are set to be $T_h = 0.90\ T_c$, $T_l = 0.82\ T_c$, and the contact angle of the hydrophilic pillars are 70°. We can see that the wick with unevenly-spaced pillar has the best performance to feed the working fluid

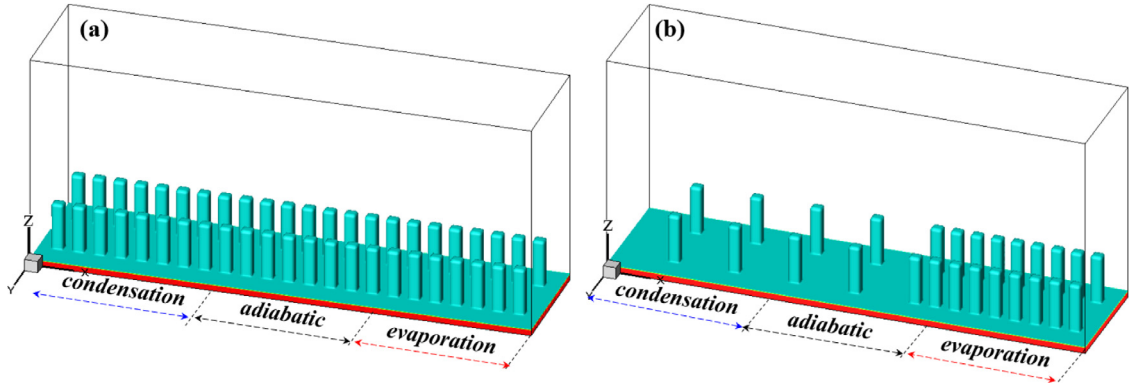

Fig. 10. Configurations of the pillar-type wicks (a) evenly-spaced pillar-type wick (b) unevenly-spaced pillar-type wick.

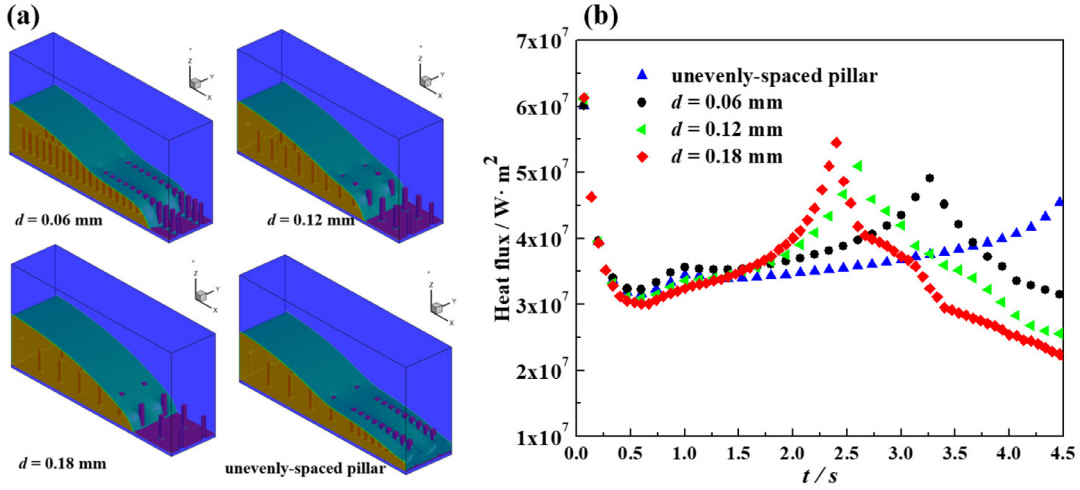

Fig. 11. Effects of the pillar configuration on the performance of the heat pipe (a) Working liquid distributions of different pillar configurations (time instant $t = 4.5$ s) (b) Comparisons of the averaged heat flux among different pillar configurations (unevenly-spaced pillar with $d = 0.06$ mm at the evaporation section and $d = 0.18$ mm at the condensation section).

from the condensation section, which the evenly-spaced pillar wick with $d = 0.18$ mm is the worst. It is because the smaller pillar pitch at the evaporation section can provide a larger capillary driven force while a sparse pillar pitch at the condensation and adiabatic section can reduce the liquid flow resistance. Fig. 11(b) shows the comparisons of averaged heat flux among different pillar configurations. It can be seen that the working fluids start to dry out at around $t = 2.4$ s, $t = 2.6$ s and $t = 3.2$ s for pillar pitch $d = 0.06$ mm, $d = 0.12$ mm and $d = 0.18$ mm, respectively.

4. Conclusions

In this paper, a three-dimensional liquid-vapor phase change LB model is developed to investigate the transient thermal performance of the flat micro heat pipe. The free surface curvature at the liquid-vapor interface can be automatically adjusted according to the environment temperature and no any empirical model of interfacial mass flux is needed. The pore scale model helps to elucidate how the wick microstructures affect the thermal performance of the flat micro heat pipe. The grooved-type wicks and micro-pillar type wicks are studied and effects of wettability, working temperature, liquid charge amount are investigated. The conclusions are as follows:

(1) For the rectangular grooved wicks, the microstructure with a better hydrophilic property can generate a higher capillary pressure difference to drive working fluid from the condensation section to the evaporation section. The wick with a lower liquid charge amount of working fluid can have a larger heat flux at the steady state.
(2) The averaged heat flux can be enhanced due to the receding of working fluid in the evaporation section but then decreases rapidly due to the occurrence of the drying out of the working fluid if the external heat source exceeds the capillary limit.
(3) For grooved-type wick, the groove with a trapezoid shape can produce the largest capillary driving force, next by the rectangular shape and then the inverse trapezoid shape. For the micro-pillar type wick, with a small pillar pitch at the evaporation section and a large pitch at the condensation section can improve the capillary limit of the heat pipe.

Declaration of Competing Interest

We wish to confirm that there are no known conflicts of interest associated with this publication and there has been no significant financial support for this work that could have influenced its outcome. We confirm that the manuscript has been read and approved by all named authors and that there are no other persons who satisfied the criteria for authorship but are not listed. We further confirm that the order of authors listed in the manuscript has been approved by all of us. We confirm that we have given due consideration to the protection of intellectual property associated with this work and that there are no impediments to publication, including the timing of publication, with respect to intellectual property. In so doing we confirm that we have followed the regulations of our institutions concerning intellectual property.

Acknowledgement

This research was supported by the Key Project of International Joint Research of National Natural Science Foundation of China (51320105004)

References

[1] A. Faghri, Review and advances in heat pipe science and technology, J. Heat Transf. 134 (12) (2012) 123001.
[2] L. Vasiliev, Micro and miniature heat pipes–electronic component coolers, Appl. Therm. Eng. 28 (4) (2008) 266–273.
[3] K.H. Do, S.J. Kim, S.V. Garimella, A mathematical model for analyzing the thermal characteristics of a flat micro heat pipe with a grooved wick, Int. J. Heat Mass Transf. 51 (19–20) (2008) 4637–4650.
[4] X. Chen, H. Ye, X. 315, T. Ren, G. Zhang, A review of small heat pipes for electronics, Appl. Therm. Eng. 96 (2016) 1–17.
[5] N. Zhu, K. Vafai, Analytical modeling of the startup characteristics of asymmetrical flat-plate and disk-shaped heat pipes, Int. J. Heat Mass Transf. 41 (17) (1998) 2619–2637.
[6] P. Mistry, F. Thakkar, S. De, S. DasGupta, Experimental validation of a two-dimensional model of the transient and steady-state characteristics of a wicked heat pipe, Exp. Heat Transf. 23 (4) (2010) 333–348.
[7] M. Mahdavi, S. Qiu, S. Tiari, Numerical investigation of hydrodynamics and thermal performance of a specially configured heat pipe for high-temperature thermal energy storage systems, Appl. Therm. Eng. 81 (2015) 325–337.
[8] B. Xiao, A. Faghri, A three-dimensional thermal-fluid analysis of flat heat pipes, Int. J. Heat Mass Transf. 51 (11–12) (2008) 3113–3126.
[9] F. Lefevre, M. Lallemand, Coupled thermal and hydrodynamic models of flat micro heat pipes for the cooling of multiple electronic components, Int. J. Heat Mass Transf. 49 (7–8) (2006) 1375–1383.
[10] Y. Cao, A. Faghri, Transient two-dimensional compressible analysis for high-temperature heat pipes with pulsed heat input, Numer. Heat Transf. 18 (4) (1991) 483–502.
[11] Z. Zuo, A. Faghri, A network thermodynamic analysis of the heat pipe, Int. J. Heat Mass Transf. 41 (11) (1998) 1473–1484.
[12] Y. Xuan, Y. Hong, Q. Li, Investigation on transient behaviors of flat plate heat pipes, Exp. Therm. Fluid Sci. 28 (2–3) (2004) 249–255.
[13] Y. Huang, Q. Chen, A numerical model for transient simulation of porous wicked heat pipes by lattice Boltzmann method, Int. J. Heat Mass Transf. 105 (2017) 270–278.
[14] U. Vadakkan, S.V. Garimella, J.Y. Murthy, Transport in flat heat pipes at high heat fluxes from multiple discrete sources, J. Heat Transf. 126 (3) (2004) 347–354.
[15] G. Carbajal, C. Sobhan, D. Queheillalt, H.N. Wadley, A quasi-3D analysis of the thermal performance of a flat heat pipe, Int. J. Heat Mass Transf. 50 (21–22) (2007) 4286–4296.
[16] S. Harmand, R. Sonan, M. Fakès, H. Hassan, Transient cooling of electronic components by flat heat pipes, Appl. Therm. Eng. 31 (11–12) (2011) 1877–1885.
[17] R. Ranjan, J.Y. Murthy, S.V. Garimella, U. Vadakkan, A numerical model for transport in flat heat pipes considering wick microstructure effects, Int. J. Heat Mass Transf. 54 (1–3) (2011) 153–168.
[18] M. Famouri, G. Carbajal, C. Li, Transient analysis of heat transfer and fluid flow in a polymer-based micro flat heat pipe with hybrid wicks, Int. J. Heat Mass Transf. 70 (2014) 545–555.
[19] J. Rice, A. Faghri, Analysis of porous wick heat pipes, including capillary dry-out limitations, in: ASME 2005 International Mechanical Engineering Congress and Exposition, American Society of Mechanical Engineers, 2005, pp. 595–607.
[20] R. Ranjan, J.Y. Murthy, S.V. Garimella, A microscale model for thin-film evaporation in capillary wick structures, Int. J. Heat Mass Transf. 54 (1–3) (2011) 169–179.
[21] R. Marek, J. Straub, Analysis of the evaporation coefficient and the condensation coefficient of water, Int. J. Heat Mass Transf. 44 (1) (2001) 39–53.
[22] F. Xin, T. Ma, Q. Wang, Thermal performance analysis of flat heat pipe with graded mini-grooves wick, Appl. Energy 228 (2018) 2129–2139.
[23] Q. Li, K. Zhao, Y. Xuan, Simulation of flow and heat transfer with evaporation in a porous wick of a CPL evaporator on pore scale by lattice Boltzmann method, Int. J. Heat Mass Transf. 54 (13–14) (2011) 2890–2901.
[24] G. Hazi, A. Markus, On the bubble departure diameter and release frequency based on numerical simulation results, Int. J. Heat Mass Transf. 52 (5–6) (2009) 1472–1480.
[25] S. Gong, P. Cheng, A lattice Boltzmann method for simulation of liquid–vapor phase-change heat transfer, Int. J. Heat Mass Transf. 55 (17–18) (2012) 4923–4927.
[26] W.Z. Fang, L. Chen, Q.J. Kang, W.Q. Tao, Lattice Boltzmann modeling of pool boiling with large liquid-gas density ratio, Int. J. Therm. Sci. 114 (2017) 172–183.
[27] L. Mottet, T. Coquard, M. Prat, Three dimensional liquid and vapour distribution in the wick of capillary evaporators, Int. J. Heat Mass Transf. 83 (2015) 636–651.
[28] M. Nishikawara, H. Nagano, M. Prat, Numerical study on heat-transfer characteristics of loop heat pipe evaporator using three-dimensional pore network model, Appl. Therm. Eng. 126 (2017) 1098–1106.
[29] J. Li, F. Hong, R. Xie, P. Cheng, Pore scale simulation of evaporation in a porous wick of a loop heat pipe flat evaporator using Lattice Boltzmann method, Int. Commun. Heat Mass Transf. 102 (2019) 22–33.
[30] W.Z. Fang, H. Zhang, L. Chen, W.Q. Tao, Numerical predictions of thermal conductivities for the silica aerogel and its composites, Appl. Therm. Eng. 115 (2017) 1277–1286.
[31] W.Z. Fang, J.J. Gou, L. Chen, W.Q. Tao, A multi-block lattice Boltzmann method for the thermal contact resistance at the interface of two solids, Appl. Therm. Eng. 138 (2018) 122–132.
[32] W.Z. Fang, Y.Q. Tang, L. Chen, Q.J. Kang, W.Q. Tao, Influences of the perforation on effective transport properties of gas diffusion layers, Int. J. Heat Mass Transf. 126 (2018) 243–255.

[33] S. Chen, G.D. Doolen, Lattice Boltzmann method for fluid flows, Annu. Rev. Fluid Mech. 30 (1) (1998) 329–364.
[34] A. Xu, W. Shyy, T. Zhao, Lattice Boltzmann modeling of transport phenomena in fuel cells and flow batteries, Acta Mech. Sin. 33 (3) (2017) 555–574.
[35] F. Lefèvre, R. Rullière, G. Pandraud, M. Lallemand, Prediction of the temperature field in flat plate heat pipes with micro-grooves–experimental validation, Int. J. Heat Mass Transf. 51 (15–16) (2008) 4083–4094.
[36] X. Xie, Q. Weng, Z. Luo, J. Long, X. Wei, Thermal performance of the flat micro-heat pipe with the wettability gradient surface by laser fabrication, Int. J. Heat Mass Transf. 125 (2018) 658–669.
[37] H. Tang, Y. Tang, Z. Wan, J. Li, W. Yuan, L. Lu, Y. Li, K. Tang, Review of applications and developments of ultra-thin micro heat pipes for electronic cooling, Appl. Energy 223 (2018) 383–400.
[38] C. Zhang, F. Hong, P. Cheng, Simulation of liquid thin film evaporation and boiling on a heated hydrophilic microstructured surface by Lattice Boltzmann method, Int. J. Heat Mass Transf. 86 (2015) 629–638.
[39] D. Zhang, K. Papadikis, S. Gu, Three-dimensional multi-relaxation time lattice-Boltzmann model for the drop impact on a dry surface at large density ratio, Int. J. Multiphase Flow 64 (2014) 11–18.
[40] Q. Li, K. Luo, X. Li, Lattice Boltzmann modeling of multiphase flows at large density ratio with an improved pseudopotential model, Phys. Rev. E 87 (5) (2013) 053301.
[41] A. Xu, T. Zhao, L. An, L. Shi, A three-dimensional pseudo-potential-based lattice Boltzmann model for multiphase flows with large density ratio and variable surface tension, Int. J. Heat Fluid Flow 56 (2015) 261–271.
[42] Y.T. Mu, L. Chen, Y.L. He, Q.J. Kang, W.Q. Tao, Nucleate boiling performance evaluation of cavities at mesoscale level, Int. J. Heat Mass Transf. 106 (2017) 708–719.
[43] Cem Ö, A.B. Uygur, I. Horuz, The effect of manufacturing limitations on groove design and its implementation to an algorithm for determining heat transport capability of heat pipes, Isı Bilimi ve Tekniği Dergisi 38 (1) (2017) 159–170.
[44] F.o. Ternet, H. Louahlia-Gualous, S.p. Le Masson, Impact of microgroove shape on flat miniature heat pipe efficiency, Entropy 20 (1) (2018) 44.